PAPER • OPEN ACCESS

Edge and core impurity behavior and transport in EAST H-mode plasma with internal transport barrier

OPEN ACCESS
IOP Publishing | International Atomic Energy Agency
Nuclear Fusion
Nucl. Fusion **65** (2025) 052003 (16pp)
https://doi.org/10.1088/1741-4326/adcbc1

Edge and core impurity behavior and transport in EAST H-mode plasma with internal transport barrier

Wenmin Zhang[1,2], Ling Zhang[1,*], Yuqi Chu[1,3,*], Shigeru Morita[1,4], Xiang Gao[1], Gongshun Li[1], Shouxin Wang[1], Yunxin Cheng[1], Yingying Li[5], Ailan Hu[1], Chengxi Zhou[1], Darío Mitnik[6], Zhen Zhou[1,2], Hailin Zhao[1], Qing Zang[1], Ning Yan[1], Jihui Chen[1], Yinxian Jie[1], Jinping Qian[1], Haiqing Liu[1], Guosheng Xu[1], Jiansheng Hu[1] and Yuntao Song[1]

[1] Institute of Plasma Physics, Hefei Institutes of Physical Science. Chinese Academy of Sciences, Hefei 230031, China
[2] University of Science and Technology of China, Hefei 230026, China
[3] University of California Los Angeles, Los Angeles, CA 90095, United States of America
[4] National Institute for Fusion Science, Toki, 509-5292 Gifu, Japan
[5] Hebei Key Laboratory of Compact Fusion, Langfang 065001, China
[6] Instituto de AstronomíayFísica del Espacio (CONICET-Universidad de Buenos Aires), Buenos Aires 1428, Argentina

E-mail: zhangling@ipp.ac.cn and yqchu@ipp.ac.cn

Received 20 January 2025, revised 18 March 2025
Accepted for publication 11 April 2025
Published 29 April 2025

Abstract

After installation of tungsten divertor in EAST, impurity accumulation of tungsten ions has been frequently observed in H-mode discharge with internal transport barrier (ITB) due to an enhancement of the impurity confinement inside the ITB. A strong plasma cooling induced by the tungsten impurity ions caused a collapse of the ITB formation. To study the impurity transport in high β_N discharges with ITB, temporal behaviors and radial profiles of spectral lines emitted from low- and high-Z impurity ions were analyzed. Line emissions from moderately ionized ions, e.g. O^{6+}, Fe^{17+} and Mo^{25+} locating outside the ITB ($\rho \geqslant 0.4$), maintain low intensities and remain unchanged during the ITB formation. However, line emissions from highly ionized high-Z impurity ions such as Fe^{22+}, Cu^{21+}, Cu^{25+}, Mo^{30+} and W^{26+}-W^{37+} locating inside the ITB ($\rho < 0.4$) are strongly influenced by peaking effects of electron density and ion temperature profiles. The impurity screening effect due to the ion temperature peaking is dominant during T_i-ITB phase because the line intensities of high-Z impurity ions are reduced and the radial high-Z impurity profiles are flattened. In contrast, during n_e-ITB phase accompanied by electron and ion temperature ITB, an increase in the electron density gradient from $R/L_{ne} = 3.4$–4.9 results in a significant increase in the high-Z impurity density, and leads to the impurity accumulation. Statistical analysis on the tungsten impurity density ($I_{W\text{-}UTA}/n_e$) with toroidal rotation velocity (V_{t0}) and ion temperature gradient (R/L_{Ti}) suggests that the

* Authors to whom any correspondence should be addressed.

tungsten impurity accumulation can be effectively mitigated and the $I_{\text{W-UTA}}/n_e$ can be reduced to below 18 (phs·m·s^{-1}·Sr^{-1}), when $R/L_{ne} < 3.4$, $V_{t0} < 150$ km·s^{-1} and $R/L_{Ti} > 2.5$. During two ITB phases, however, low-Z impurity ions like O^{7+} locating at edge of the ITB appear to be sensitive to only the electron density gradient.

Keywords: EAST tokamak, tungsten impurity ions, internal transport barrier, ion temperature gradient, electron density gradient, toroidal rotation velocity

(Some figures may appear in colour only in the online journal)

1. Introduction

To improve the plasma performance of future fusion devices such as SPARC [1] and ITER [2], several advanced operation modes have been adopted including hybrid and steady-state scenarios. Although these scenarios basically feature an edge transport barrier, those are often accompanied by a formation of the internal transport barrier (ITB) [3]. In the ITB region at the plasma core a steeper pressure gradient which can improve the plasma performance and an increase in the bootstrap current fraction are observed. It is expected that the formation of ITB is primarily attributed to a reduction of turbulence-driven transport, resulting in a transport coefficient near the neoclassical transport level. At present, studies on the ITB formation and its sustainment have been extensively performed in several devices, such as JET [4], Alcator C-Mod [5, 6], JT-60U [7], DIII-D [8], ASDEX Upgrade [9], KSTAR [10], HL-2A [11] and EAST [12–15]. However, impurity confinement can be also increased in the ITB region, which leads to a collapse of the ITB formation or discharge termination through the enhanced radiation loss [16]. Therefore, control of the impurity transport remains one of the critical issues in steady sustainment of ITB plasma formation.

Studies on the ITB plasma formation in tokamak and helical plasmas indicate that the impurity transport is primarily dominated by the neoclassical inward convection, of which the effect is much larger than the effect of the anomalous transport diffusion if the turbulence effect can be ignored [17–21]. For example, on DIII-D, JET, LHD, Alcator C-Mod and JT-60U ITB experiments, significant peaking impurity ions and strong impurity accumulation are observed for He, C, Ar and Ni ions when the bulk ion density profile is sharply peaked. Here, the peaked impurity profile may be driven by the inward convective velocity, of which the magnitude is proportional to the bulk ion density gradient. Furthermore, the strength of the impurity peaking increases with the charge state of the impurity ions [17, 18]. On Alcator C-Mod, the application of additional on-axis ion cyclotron resonance heating effectively suppresses the density and impurity peaking [6]. However, numerical simulations using neoclassical transport code show a discrepancy between the simulated and experimental results on impurity behavior inside the ITB, in particular, for carbon ions, suggesting the presence of turbulence or anomalous transport on low-Z impurity ions [17, 19–21]. On EAST, we simultaneously investigated behaviors of low-Z, e.g. C and O, and high-Z, e.g. Fe, Cu, Mo and W, impurity ions during high β_N discharges with ITB using extreme ultraviolet (EUV) spectrometer systems. By utilizing space-resolved EUV spectrometers, a particular attention was paid to behavior of tungsten ions because the tungsten is now materials for both divertor and first wall in ITER [22–24]. Experimental results showed a significant difference in temporal evolution behaviors between low-Z ions, e.g. O, and high-Z ions, e.g. W. Transports of both low-Z and high-Z impurity ions are significantly influenced by the electron density peaking. However, density of the high-Z impurity ions exhibits a strong correlation with toroidal rotation velocity and ion temperature gradient, while the low-Z impurity ions have less correlation against them.

The present paper describes the experimental setup in section 2 and analysis of experimental results in section 3. The effects of toroidal rotation velocity and ion temperature and electron density gradients on impurity transport during ITB formation are reported in section 4 with discussions. Finally, the paper is summarized in section 5.

2. Experimental setup

EAST is a superconducting tokamak equipped with tungsten divertor. During the period from 2014–2021, Graphite and molybdenum materials were used for lower divertor and the first wall, respectively, while iron and copper materials were employed for dedicated radio frequency heating antennas and diagnostic protection [22, 23]. Auxiliary heating systems of 2.45 GHz/4.6 GHz lower hybrid wave (LHW) and neutral beam injection (NBI) were used for operation of high β_N discharges. The NBI system consisted of four beamlines, two for co-direction and other two for ctr-direction. The toroidal magnetic field in these experiments ranged in B_t ∼—(1.6–1.8) T, where the minus sign indicates clockwise B_t direction. The magnetic configuration of upper single null (USN) was operated for the experiment with $q_{95} = 3.5$–4.0 [25].

The diagnostics utilized in this study are shown in figure 1, including several systems for plasma parameter measurement and spectroscopic systems for studying impurity behaviors. Ion temperature and toroidal rotation velocity are measured by charge exchange recombination spectroscopy (CXRS) [26]. The electron temperature profile is obtained from vertical Thomson scattering (TS) system [27]. Due to the low toroidal

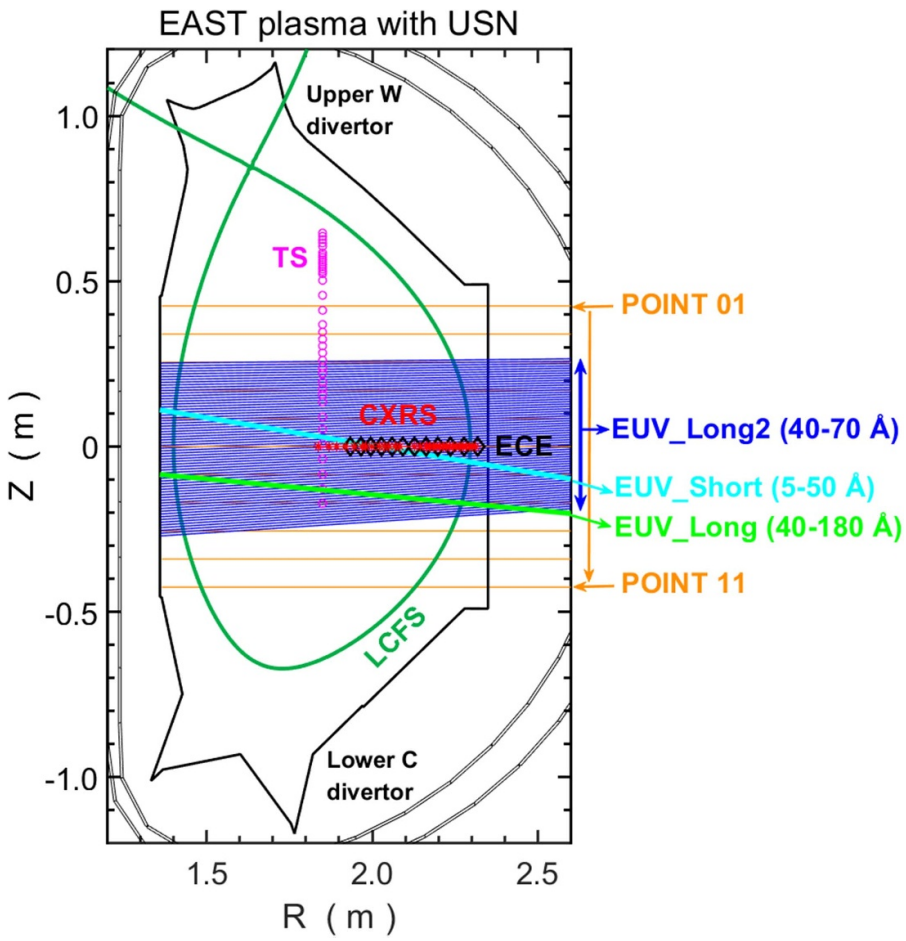

Figure 1. Cross-sectional view of EAST plasma. Typical plasma shape and arrangements of main diagnostics are illustrated with observation ranges of three extreme ultraviolet (EUV) spectrometer systems (space-resolved EUV_Long2 and fast-response EUV_Short and EUV_Long). Main diagnostics and their measured parameters include: electron density determined by polarimeter-interferometer (POINT); electron temperature obtained by Thomson scattering (TS) and electron cyclotron emission (ECE); and ion temperature and toroidal rotation velocity provided by charge exchange recombination spectrometer (CXRS).

magnetic field conditions, multichannel middle-plane electron cyclotron emission (ECE) diagnostic does not provide absolute local electron temperature [28]. Instead, the ECE signal is primarily used to observe a relative change in the electron temperature. Electron density is measured by an 11-channel polarimeter-interferometer (POINT) [29]. A temporal evolution of impurity species is monitored by two fast-time-response EUV spectrometers of EUV_Short and EUV_Long with time resolution of 5 ms/frame. The EUV_Short and EUV_Long are working at 5–50 Å and 40–180 Å, respectively. Both spectrometers have a single lines-of-sight (LOS), as shown in figure 1 [30, 31]. The radial profile of impurity line emissions is measured by a space-resolved EUV_Long2 spectrometer, of which the vertical observation range is $\Delta Z \sim 50$ cm along the Z-axis as shown in figure 1. In routine discharges, the EUV_Long2 is primarily operated to observe the wavelength range of 40–70 Å where pseudo-continuum spectrum named unresolved transition array of tungsten ions (W-UTA: W^{24+}–W^{45+}) exists. The vertical observation and wavelength ranges of the EUV_Long2 spectrometer system are adjustable, allowing a high flexibility in measuring the impurity profile [32].

3. Behavior of impurity ions in ITB discharge

3.1. Discharge #71326 with co- and ctr-NBI heating during current flat-top phase

Waveform of discharge #71326 for a representative ITB experiment is shown in figure 2, where a flat top of the plasma current of $I_p = 0.46$ MA is maintained with $B_T = -1.6$ T during the time interval of $t = 2.5$–5.5 s. The safety factor at the 95% normalized poloidal flux surface is $q_{95} = 4.1$. Table 1 summarizes the heating power values. During the plasma current flat-top phase, LHW power of P_{LHW} (4.6 GHz) = 0.95 MW is steadily injected. The NBI power is injected stepwise (see figure 2(a)). The first co-NBI beam is injected at $t = 2.5$ s with $P_{co\text{-}NBI} = 1.2$ MW and the power is increased to $P_{co\text{-}NBI} = 2.5$ MW at $t = 3.0$ s, and the ctr-NBI beam is injected at $t = 3.5$ s with $P_{ctr\text{-}NBI} = 1.0$ MW and the power is also increased to $P_{ctr\text{-}NBI} = 2.2$ MW at $t = 4.0$ s. After the first co-NBI injection at $t = 2.5$ s, the D_α emission shown in figure 2(b) indicates edge localized mode (ELM) events due to L-H transition. High normalized beta values ($\beta_N = 1.5 \sim 2.0$) are sustained between $t = 3.60 \sim 4.69$ s. Magnetohydrodynamic

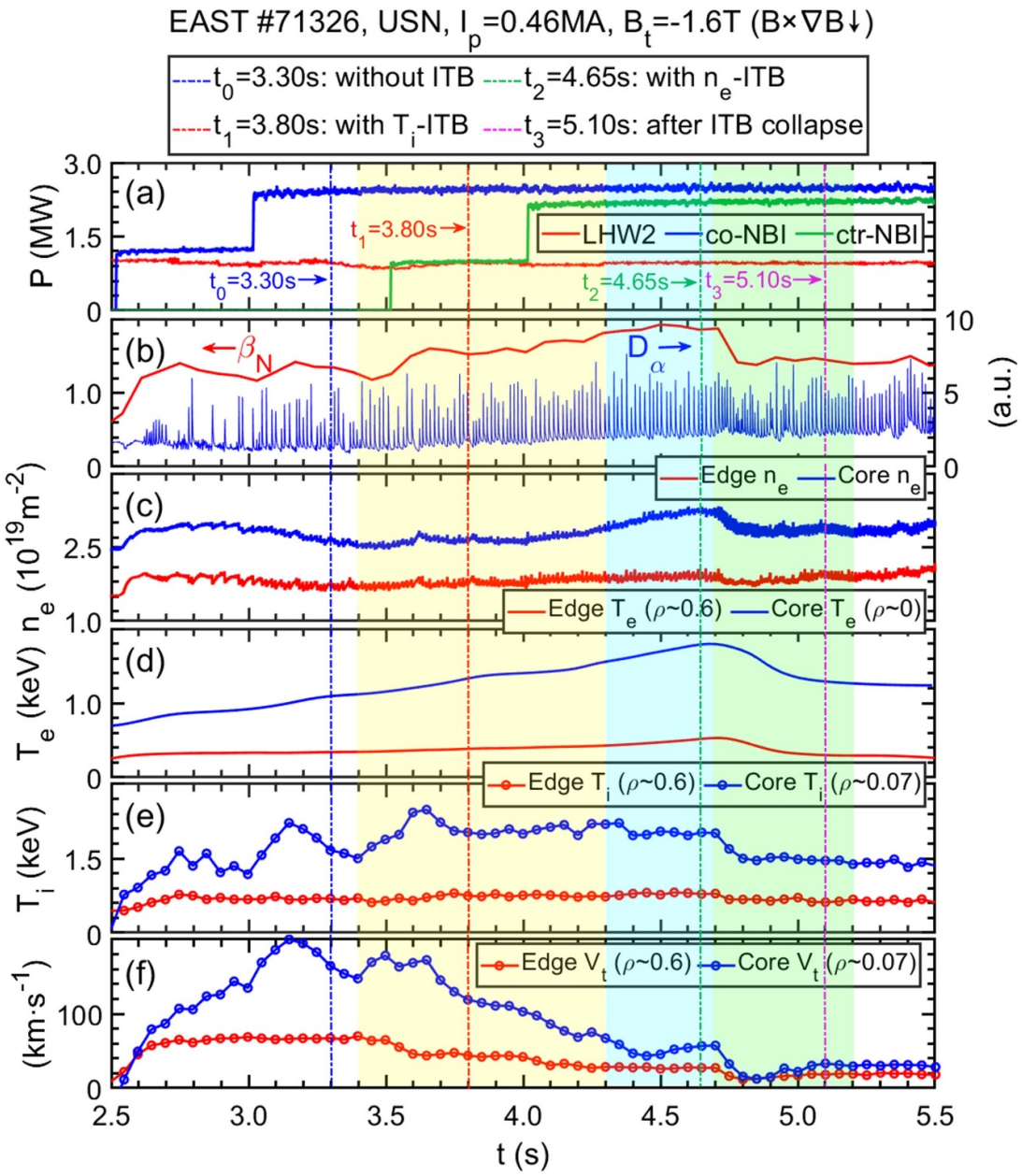

Figure 2. Typical waveforms of #71326 discharge with internal transport barrier (ITB): (*a*) heating power of 4.6 GHz lower hybrid wave ($P_{\rm LHW}$: LHW2) and neutral beams ($P_{\rm co\text{-}NBI}$: co-NBI and $P_{\rm ctr\text{-}NBI}$: ctr-NBI), (*b*) normalized beta $\beta_{\rm N}$ and D_α emission, (*c*) line-integrated electron density, $n_{\rm e}$, measured by POINT, (*d*) electron temperature, $T_{\rm e}$, obtained by ECE, (*e*) ion temperature, $T_{\rm i}$, and (*f*) toroidal rotation velocity, $V_{\rm t}$, determined by CXRS. Yellow-shaded area indicates time period of the $T_{\rm i}$-ITB formation at $t = 3.40$–4.30 s. Cyan-shaded area indicates time period of $n_{\rm e}$-ITB with $T_{\rm i}$-ITB and $T_{\rm e}$-ITB at $t = 4.30$–4.69 s. Green-shaded area denotes time period after ITB collapse at $t = 4.69$–5.20 s. Vertical dash-dotted lines in blue, red, green and magenta indicate timings at $t = 3.30$ s (without ITB), 3.80 s ($T_{\rm i}$-ITB), 4.65 s ($n_{\rm e}$-ITB with $T_{\rm i}$-ITB and $T_{\rm e}$-ITB) and 5.10 s (ITB collapse), respectively.

instabilities are analyzed at the high $\beta_{\rm N}$ phase as shown in [13, 33].

Figure 3 shows radial profiles of $n_{\rm e}$, $T_{\rm e}$, $T_{\rm i}$ and $V_{\rm t}$ at four specific time slices during the NBI-dominated heating H-mode phase, at which the timing is indicated by four vertical dash-dotted lines in figure 2. It is noted here that the radial profile measurements of $T_{\rm i}$ and $V_{\rm t}$ are available only at $\rho < 0.6$. Time evolutions of $n_{\rm e}$, $T_{\rm e}$, and $T_{\rm i}$ in figures 2(*c*)–(*e*) and radial profiles of $n_{\rm e}$, $T_{\rm e}$, and $T_{\rm i}$ indicate formation of the ITB. The core line-integrated electron density gradually increases from $t = 4.30$ s, following the injection of additional ctr-NBI beam at $t = 4.0$ s. During the core density increase phase, the edge line-integrated electron density is unchanged, suggesting formation of density transport barrier followed by the density peaking. As shown in figure 3(*a*), the $n_{\rm e}$ profile at $t = 4.65$ s is significantly peaked at $\rho < 0.4$ ($(R/L_{ne})_{\rm max} = 4.9$), compared to that at $t = 3.30$ s ($(R/L_{ne})_{\rm max} = 2.7$) and $t = 3.80$ s ($(R/L_{ne})_{\rm max} = 3.4$). However, after $t = 4.69$ s at which the double tearing mode seems to change to the kink mode, the core density peaking is broken, indicating collapse of the

Table 1. Heating power for EAST discharges #71326 and #80839.

Heating	Shot	EAST #71326		EAST #80839	
		Time interval (s)	Power (MW)	Time interval (s)	Power (MW)
LHW		1.9–8.0	0.95	1.6–7.4	0.8
co-NBI	NBI1L	2.5–7.5	1.2	3.0–7.0	1.0
	NBI1R	3.0–7.0	1.3	3.3–7.3	1.1
ctr-NBI	NBI2L	3.5–6.5	1.0		
	NBI2R	4.0–6.0	1.2		

density barrier. Therefore, there is an electron density barrier (n_e-ITB) formation at $t = 4.30$–4.69 s.

Radial profile of T_e shown in figure 3(*b*) clearly indicates formation of the T_e-ITB at $t = 4.65$ s, while a weak T_e-ITB formation is observed at $t = 3.80$ s. Calculation using TRANSP code strongly suggests that the T_e-ITB formation is closely associated with a significant reduction in the electron thermal transport [13]. In addition, the time evolution of T_i in figure 2(*e*) and radial profiles of T_i in figure 3(*c*) indicates that a clear formation of the T_i-ITB after the second ctr-NBI beam injection at $t = 3.50$ s. This T_i-ITB formation is collapsed at $t = 4.69$ s as well as the T_e-ITB formation. The toroidal rotation velocity plotted in figure 2(*f*) increases with the co-NBI injection, whereas it is significantly suppressed with the ctr-NBI injection. As shown in figure 3(*d*), the toroidal velocity profile collapses following the application of the ctr-NBI. Therefore, during the time interval of 3.40–4.30 s, a transport barrier was formed only in the ion temperature channel (T_i-ITB); whereas in the interval of 4.30–4.69 s, transport barriers were observed simultaneously in the electron density (n_e-ITB), electron temperature (T_e-ITB), and ion temperature (T_i-ITB) channels. The four time slices are finally chosen for the following data analysis, i.e. $t = 3.30$ s (blue lines: without ITB), $t = 3.80$ s (red lines: with T_i-ITB), $t = 4.65$ s (green lines: with n_e-ITB, T_i-ITB and T_e-ITB) and $t = 5.10$ s (magenta lines: after ITB collapse). The corresponding dimensionless parameters, $\eta_e = \mathrm{dln}T_e/\mathrm{dln}n_e$ and $\eta_i = \mathrm{dln}T_i/\mathrm{dln}n_i$, are shown in figures 3(*e*) and (*f*), respectively. In our study, the primary gas is deuterium, and the concentration of impurity ions in the main plasma is much lower than that of the main ions (n_i). Due to the lack of measurement for the n_i distribution on EAST, we approximate the n_i to be equal to the n_e based on the quasi-neutrality condition. Therefore, we calculated η_i as $\eta_i \sim \mathrm{dln}T_i/\mathrm{dln}n_e$.

3.2. Temporal behavior of low-Z impurity ions in ITB discharge

Figure 4 illustrates the temporal variation of line emissions from intrinsic impurity ions (low-Z: C and O, high-Z: Fe, Cu, Mo and W) in #71326 discharge with ITB formation. The shaded areas in yellow, cyan and green colors denote different ITB phases as mentioned above. Before the ITB formation until $t = 3.4$ s, the line emission intensity of C^{4+} remains nearly constant, while the intensity of C^{5+}, O^{6+}, and O^{7+} increases significantly. During the T_i-ITB formation of $t = 3.4$–4.3 s, the line emission intensity of C^{4+} and O^{6+} still remains stable, while the line emission intensity of C^{5+} and O^{7+} increases slightly, which is likely associated with increase in the electron density. Meanwhile, this also indicates that such changes in impurity emissions are not caused by the increase in edge impurity sources. Subsequently, when the plasma enters the n_e-ITB phase at $t = 4.3$ s, the line emission intensity of O^{7+} rapidly increases, likely primarily influenced by the formation of the n_e-ITB, while the line emission intensity of O^{6+} is unchanged. Similar to this, the line intensity of C^{5+} slightly increases, while the line intensity of C^{4+} is unchanged. Based on the radial profile measurement, it is known that C^{4+} and C^{5+} ions are primarily localized in the pedestal region at $\rho > 0.9$ and the pedestal top near $\rho = 0.9$, respectively. The O^{6+} ions are primarily located at the region between the pedestal top and ITB foot, whereas the O^{7+} ions are mainly concentrated inside the ITB. After the ITB collapsed at $t = 4.69$ s, the emission intensity of C^{5+} began to decrease with a delay time of $\Delta t = 0.086$ s ($t = 4.776$ s), while the O^{7+} emission intensity drops sharply with a delay time of $\Delta t = 0.166$ s ($t = 4.856$ s).

3.3. Temporal behavior of high-Z impurity ions in ITB discharge

In discharge #71326 the EUV_Long spectrometer was operated in the wavelength range of 40–180 Å to cover all impurity spectra analyzed in this section. Before the formation of the T_i-ITB the value of T_e is lower than the ionization equilibrium temperature for high-Z impurity ions of Cu^{21+}, Cu^{25+} and Mo^{30+}. As a result, the line emissions from these impurity ions are not basically observable at $t = 2.50$–3.60 s, as shown in figures 4(*d*) and (*e*). After the plasma enters the T_i-ITB phase, the line emission from such ions begins to increase with increase in T_{e0} from 1.0 keV to 1.4 keV during $t = 3.40$–3.80 s. Since Fe^{22+}, Cu^{25+} and Mo^{30+} ions mean the highest ionization stage of their impurity species in this discharge, those ions are primarily localized in the central region of plasma and predominantly confined inside the ITB. The T_i-ITB induced the temperature screening effect dominates the impurity transport in the time interval of $t = 3.8$–4.3 s. For example, the line emission of Fe^{17+} remains nearly constant, while that of

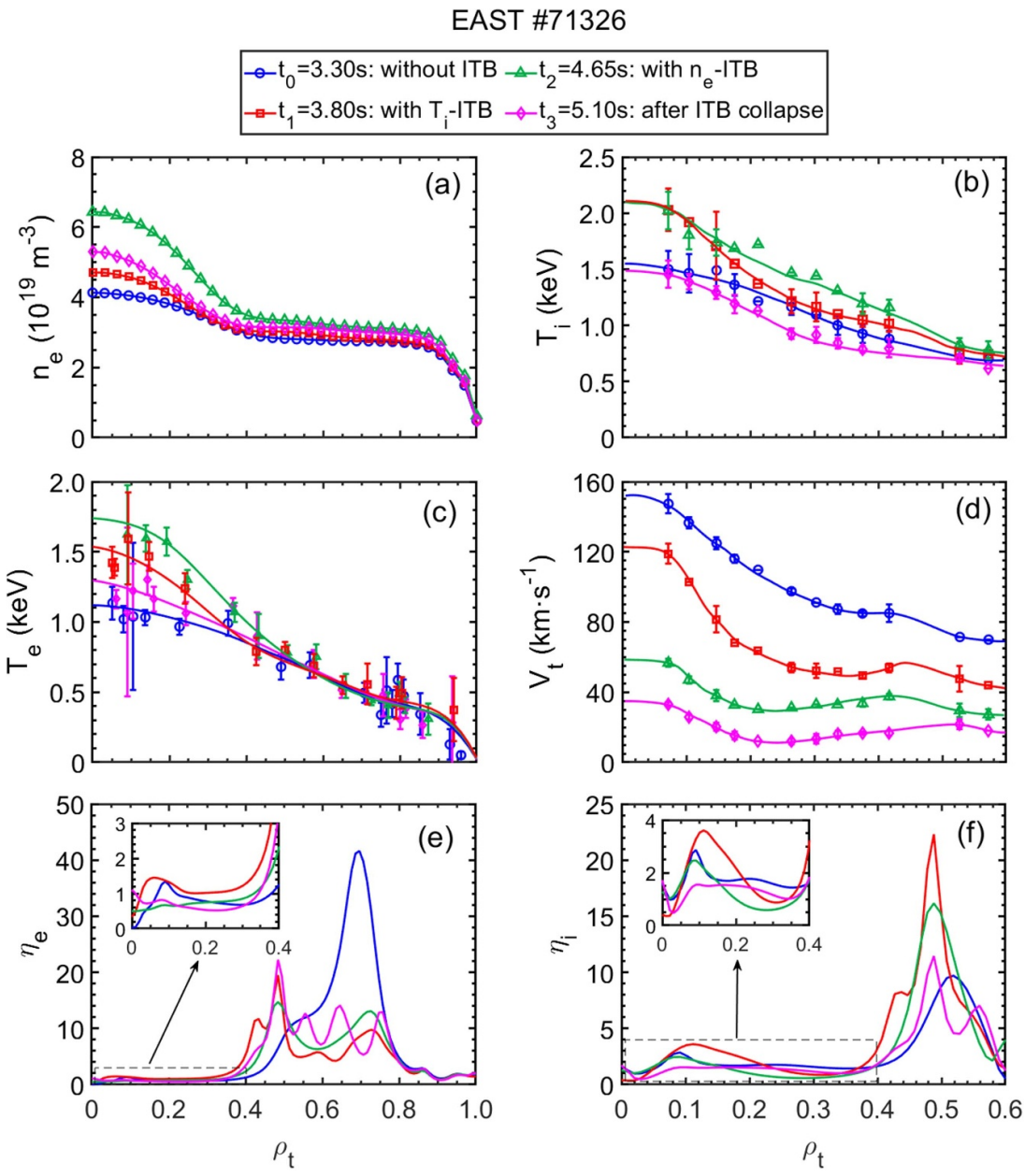

Figure 3. Radial profiles of (*a*) electron density, n_e, measured by POINT, (*b*) ion temperature, T_i, obtained by CXRS, (*c*) electron temperature, T_e, determined by TS, (*d*) toroidal rotation velocity, V_t, provided by CXRS, (*e*) ratio of logarithmic gradient of electron temperature to logarithmic gradient of density, η_e, and (*d*) ratio of logarithmic gradient of ion temperature to logarithmic gradient of density, η_i, at four timings in EAST #71326 discharge. Four discharge timings are indicated in figure 2 with vertical dash-dotted lines.

Fe^{22+} decreases the intensity. When the plasma enters the n_e-ITB phase (t = 4.30–4.69 s), the line emission of Fe^{17+} still remains stable, while that of Fe^{22+} ions rapidly increase the intensity by 70%. During both phases, the intensity of Mo^{25+} ions is unchanged similar to the Fe^{17+} ions, while the intensity of Cu^{21+}, Cu^{25+} and Mo^{30+} shows a similar behavior to the Fe^{22+} ions. These observations indicate that line emissions of Cu^{21+}, Cu^{25+}, Mo^{30+} and Fe^{22+} ions with higher ionization energies locating inside the ITB are strongly affected by the ITB formation, whereas line emissions of Fe^{17+} and Mo^{25+} ions with relatively lower ionization energies locating in the region between ITB foot and pedestal top are unchanged during the ITB.

When the plasma enters the H-mode and the toroidal rotation velocity in the plasma center rapidly increases to 200 km·s^{-1} (see figure 2(*f*)), the tungsten line emission of W^{27+} and W^{32+} ions significantly increase as plotted in figure 4(*f*). However, once the T_i-ITB is formed (t = 3.40–3.60 s), the line emission quickly decreases by approximately 60%. The reduction of the tungsten line emission continues until t = 4.30 s. When the n_e-ITB is formed (t = 4.30–4.69 s), the line emission of W^{27+} and W^{32+} ions starts to increase again. The W^{32+} ions locating at the plasma center show a pronounced increase compared to the W^{27+} ions. The temporal evolutions of W^{27+} and W^{32+} ions during the ITB formation exhibits a similar behavior to those of Fe^{22+}, Cu^{21+},

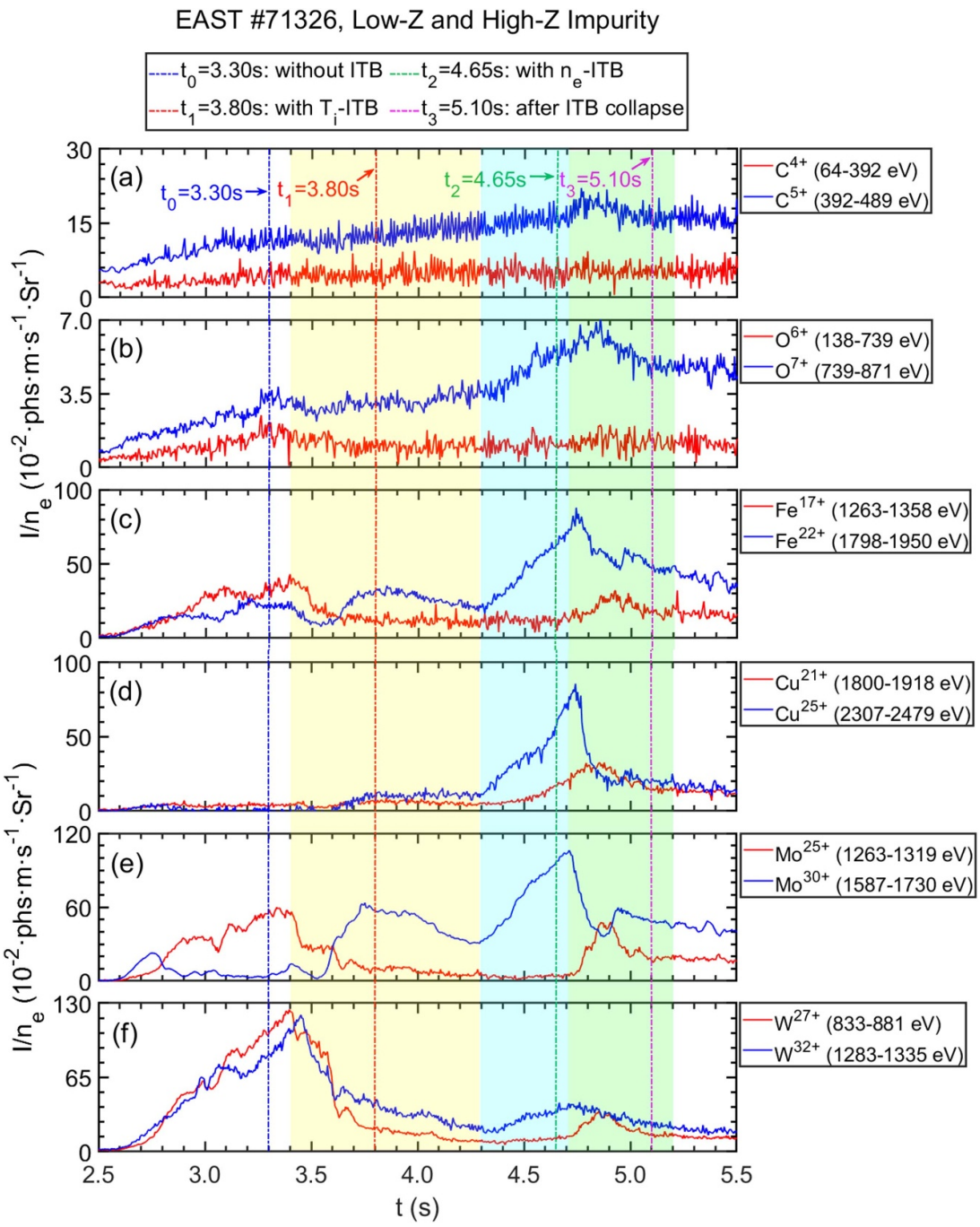

Figure 4. Temporal line intensity evolutions of low- and high-Z impurity ions: (*a*) C^{4+} (ionization energy interval: $E_i(Z-1)$–$E_i(Z)$ eV) at 40.268 Å and C^{5+} at 33.734 Å, (*b*) O^{6+} at 21.602 Å and O^{7+} at 18.970 Å, (*c*) Fe^{17+} 93.926 Å and Fe^{22+} at 132.980 Å, (*d*) Cu^{21+} at 90.276 Å and Cu^{25+} at 111.186 Å, (*e*) Mo^{25+} at 76.624 Å and Mo^{30+} at 115.999 Å, and (*f*) W^{27+} at 49.403 Å and W^{32+} at 52.20 Å. The three shaded areas and four vertical dash-dotted lines have the same meanings as those in figure 2.

Cu^{22+} and Mo^{30+} ions. It indicates that transport of the tungsten ions locating in the plasma core is also affected by the ITB formation. After the collapse of the ITB at $t = 4.69$ s, the evolution of impurity ions exhibited notable differences. In particular, the temporal behavior of the same impurity species at various ionization stages, e.g. Fe^{17+} and Fe^{22+}, Cu^{21+} and Cu^{25+}, Mo^{25+} and Mo^{30+}, W^{27+} and W^{32+}, was distinctly different. Similar temporal evolutions had also been observed in low-Z impurities, e.g. C^{4+} and C^{5+}, O^{6+} and O^{7+}. This phenomenon is attributed to the collapse of the ITB, which causes highly ionized impurity ions to be ejected from the plasma core and undergoes recombination processes with electrons, leading to the formation of lower-ionized states of impurity ions. As a result, we observe a sequential enhancement in the emission of moderately charged impurity ions.

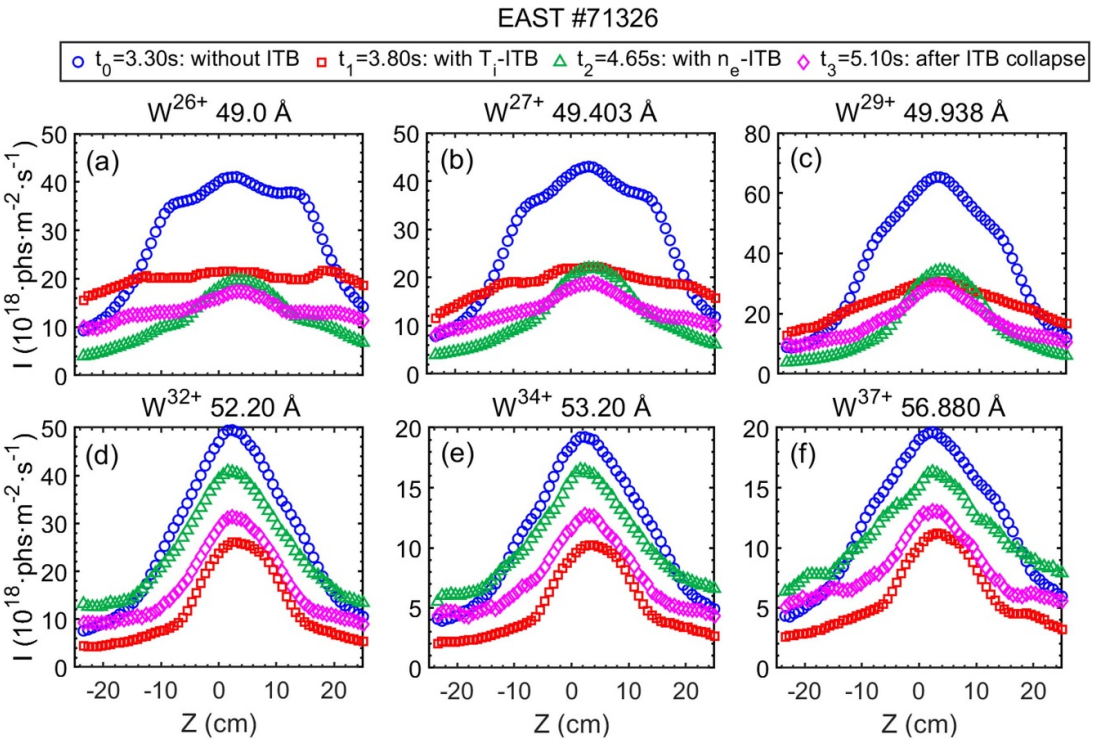

Figure 5. Vertical intensity profiles of tungsten impurity ions measured by EUV_Long2 spectrometer in EAST discharge #71326: (*a*) W^{26+} (784–833 eV) at 49.0 Å, (*b*) W^{27+} (833–881 eV) at 49.403 Å, (*c*) W^{29+} (1132–1180 eV) at 49.938 Å, (*d*) W^{32+} (1283–1335 eV) at 52.20 Å, (*e*) W^{34+} (1387–1460 eV) at 53.2 Å, and (*f*) W^{37+} (1569–1622 eV) at 56.880 Å observed at four timings shown in figures 2 and 3.

3.4. Radial profiles of tungsten impurity ions in ITB discharge

Figure 5 shows vertical intensity profiles of W^{26+} at 49.0 Å, W^{27+} at 49.403 Å, W^{29+} at 49.938 Å, W^{32+} at 52.20 Å, W^{34+} at 53.20 Å, and W^{37+} at 56.880 Å in #71326 at four time slices. Before the ITB formation ($t = 3.30$ s), the profiles of W^{26+}, W^{27+} and W^{29+} show a significant accumulation, and the tungsten ions in higher ionization stages of W^{32+}, W^{34+} and W^{37+} simply exhibits a peaked profile. After the discharge enters the T_i-ITB phase ($t = 3.80$ s), the line emissions of W^{26+}, W^{27+} and W^{29+} ions decrease significantly, and their profiles become flatter. This indicates that the formation of the T_i-ITB can effectively suppress the tungsten accumulation and reduce the tungsten content inside the T_i-ITB. During the phase of n_e-ITB at $t = 4.65$ s, the impurity accumulation is observed at $\rho < 0.1$, although the overall emission intensities of W^{26+}, W^{27+}, and W^{29+} ions decrease compared to the T_i-ITB phase at $t = 3.80$ s. The tungsten accumulation during n_e-ITB can be attributed to fact that the formation of the n_e-ITB enhances the peaking effect of the electron density, which dominates over the screening effect of the ion temperature gradient. Compared to the η_i during the T_i-ITB, the η_i inside the ITB region significantly decreases after the n_e-ITB forms, as shown in figure 3(*f*). At the same time, the line emissions from W^{32+}, W^{34+} and W^{37+} ions increase significantly. After the collapse of the n_e-ITB at $t = 5.10$ s, the tungsten radiation in the plasma core decreases and the tungsten accumulation can be mitigated.

The density distribution of tungsten impurity ions may deviate from the vertical intensity distribution due to the impact of electron temperature and density. Therefore, it is crucial to invert the impurity density distribution. First, a collisional-radiative model is established and a coefficient matrix is constructed using transition rates and excitation rate coefficients calculated with the Flexible Atomic Code [34] to determine the photon emissivity coefficient (PEC) of impurity ions. Second, based on the vertical profile of impurity ions emission intensity, Abel inversion is combined with the equilibrium fitting code to reconstruct local emissivity profiles of the emission lines [35]. Finally, by using the measured electron density and temperature, along with the local emissivity profiles and PEC, the impurity density profiles are obtained. Therefore, as shown in figure 6, density profiles for W^{27+}, W^{29+}, and W^{37+} are obtained at $t = 3.30$ s, 3.80 s, 4.65 s, and 5.10 s because PEC data are only available for these three tungsten impurity ions. Before the formation of the ITB, a notable accumulation is observed in the density distribution of W^{27+} and W^{29+}. Following the ITB forms, the density profiles of W^{27+} and W^{29+} are relatively flat, while W^{37+} exhibits a hollow distribution. With the formation of the n_e-ITB, the η_i undergoes a substantial reduction (see figure 3(*f*)). As a result, W^{27+} and W^{29+} ions accumulate towards the plasma core, and

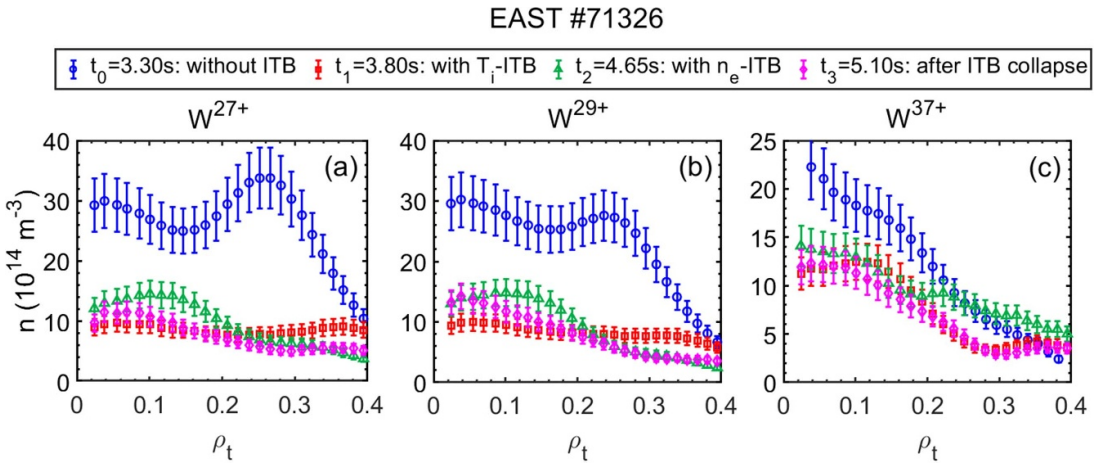

Figure 6. Density profiles of tungsten impurity ions at four timings shown in figure 5: (*a*) W^{27+}, (*b*) W^{29+}, and (*c*) W^{37+}, calculated from lines of 49.403 Å, 49.938 Å and 56.880 Å, respectively.

the distribution of W^{37+} transitions from hollow to peaked. After the collapses of ITB, the degree of peaking in tungsten impurity ions is effectively mitigated. The density distribution of tungsten impurity ions suggests that the variations in η_i may affect their distribution.

The radial profile of W^{26+}–W^{37+} ions during discharge #71326 indicate that the W-UTA is predominantly localized inside the ITB under high β_N conditions (see figures 5 and 6). In this series of experiments, it was not possible to adjust EUV_long2 during a single discharge to simultaneously observe highly ionized tungsten ions inside the ITB and low-ionized tungsten ions outside the ITB due to a limited wavelength range ($\Delta\lambda = 30$ Å) of EUV_long2 spectrometer. Then, line emissions of Mo impurity ions are used instead of the tungsten line emissions as a reference to investigate the high-Z impurity distribution outside the ITB.

In the present discharge #71326, the LOS of the EUV_Long2 spectrometer covered the radial range of $\rho < 0.3$ inside the ITB. To study the impurity distribution outside the ITB, it was necessary to change the measurement range by shifting the spectrometer LOS to the upper plasma region (-10 cm $\leqslant Z \leqslant 40$ cm). Density profiles of Mo ions are analyzed in discharge #80839, which is a typical ITB discharge with NBI-dominated heating under low toroidal magnetic field. The corresponding heating power values are provided in table 1. The temporal evolution and the profiles of T_e, n_e, and other discharge parameters before and after the formation of the n_e-ITB are shown in figures 7 and 8, respectively. The intensity profiles of Mo ions, measured by EUV_Long2 operated in 70–100 Å, are shown in figure 9. Meanwhile, the density profile of Mo ions is obtained using the same method as for W impurity ions. As shown in figure 9(*d*), following the formation of the n_e-ITB, there is a significant increase in Mo^{29+} inside the ITB, with the profile becoming more peaked for stronger n_e-ITB. Furthermore, the temporal evolution of line intensity of the Mo^{29+} ions is found to be very similar to those of Mo^{31+} and W^{32+} ions shown in figures 4(*e*) and (*f*). In contrast, the density profiles of Mo^{25+} ions remain unchanged during the n_e-ITB formation, suggesting that these ions are located outside the ITB. This observation aligns well with the temporal evolution of Mo^{25+} ions shown in figure 4(*e*). These results experimentally certify that the transport of both W and Mo ions are strongly affected by the presence of the ITB and the ITB formation gives almost no impact on the high-Z impurity ion transport locating in the region between ITB foot and pedestal top.

4. Discussions

4.1. Effects of toroidal rotation velocity and ion temperature screening

During co-NBI injection at $t = 2.5$ s and 3.0 s in discharge #71326, line emissions from high-Z impurity ions, particular tungsten ions, significantly increase, as shown in figure 10. At the same time, the toroidal rotation velocity continuously increases (see figure 10(*b*)). In contrast to this, during the ctr-NBI injection at $t = 3.5$ s and 4.0 s, the toroidal rotation velocity gradually decreases from 200 km·s^{-1} to 80 km·s^{-1} with reduction of the line emission from high-Z impurity ions (see figures 10(*b*) and (*c*)). A similar trend has been observed in the density of high-Z impurities and the toroidal rotation velocity over the period of relatively stable R/L_{Ti}. This seems to suggest the accumulation of high-Z impurities is correlated with the toroidal rotation velocity in beam heating cases [36]. To study this relationship, a statistical analysis was performed on the correlation between the two. The analysis utilizes experimental data of approximately 100 USN configuration discharges in NBI-dominant heating conditions with $B_t \sim -1.65$–-1.80 T. The tungsten density ($I_{W\text{-}UTA}/n_e$) is evaluated from the intensity of W-UTA spectrum emitted in the wavelength range of 45–70 Å and the line-averaged electron density. All data are averaged over time interval of $\Delta t = 0.1$ s during the plasma current flat-top phase. Figure 11(*a*) illustrates the relationship between V_{t0} and $I_{W\text{-}UTA}/n_e$, with their correlation analyzed using the Pearson correlation coefficient (r) and significance level (p). The results are presented in table 2. The $r = 0.743$ and $p = 1.23 \times 10^{-16}$ indicate a significant positive

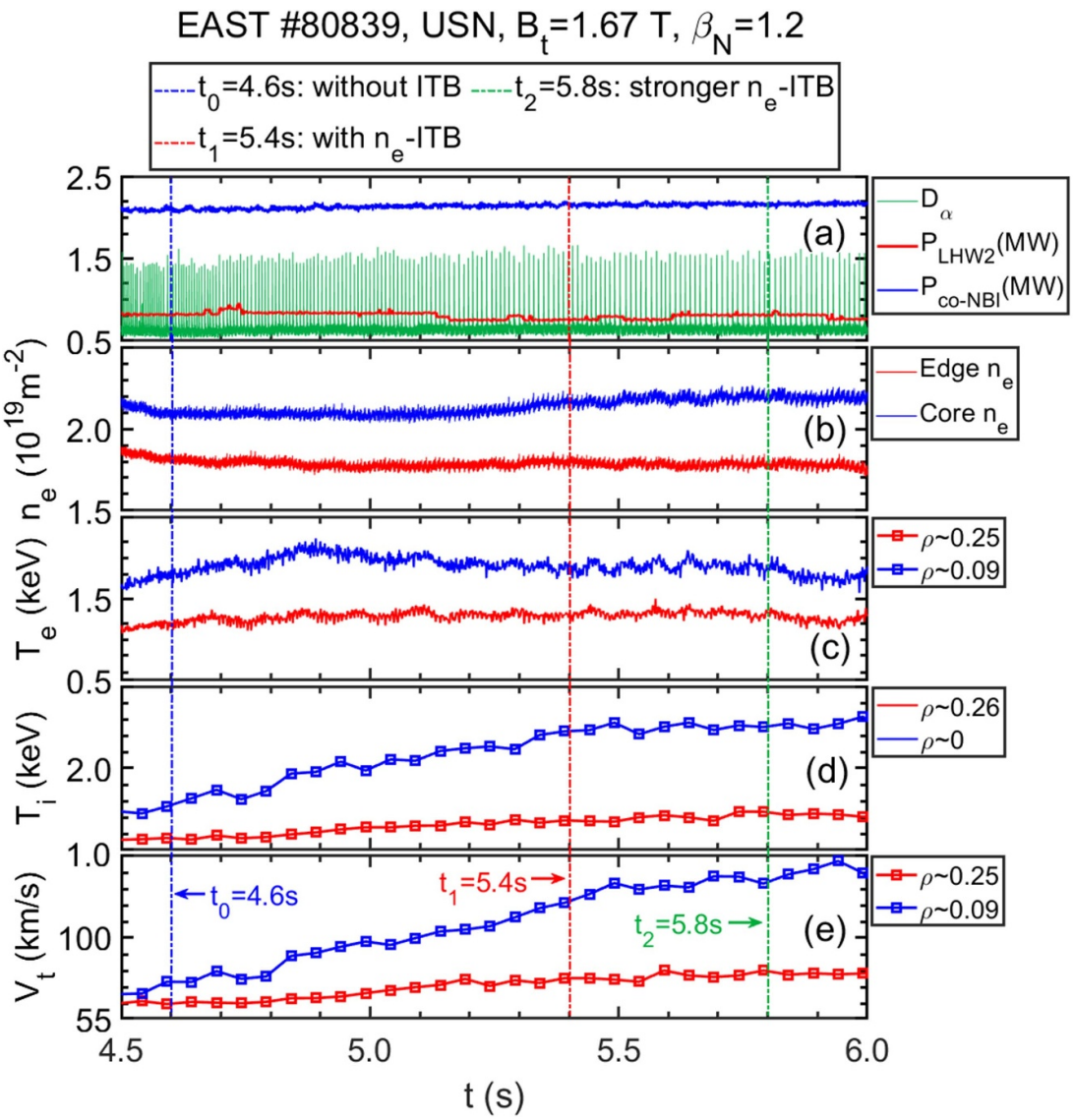

Figure 7. Time evolution of EAST discharge #80839: (*a*) D_α emission, and heating power of 4.6 GHz lower hybrid wave, P_{LHW2}, and neutral beams, $P_{\mathrm{co\text{-}NBI}}$, (*b*) line-integrated electron density, n_e, (*c*) electron temperature, T_e, (*d*) ion temperature, T_i, and (*e*) toroidal rotation velocity, V_t. Vertical dash-dotted lines in blue, red, and green indicate timings at $t = 4.6$ s (without ITB), 5.4 s (n_e-ITB with T_i-ITB and T_e-ITB), and 5.8 s (stronger n_e-ITB with T_i-ITB and T_e-ITB), respectively.

correlation trend between V_{t0} and $I_{\mathrm{W\text{-}UTA}}/n_\mathrm{e}$. However, this trend is affected by variations in experimental parameters, including electron density, ion temperature, heating power, and tungsten impurity source content. In addition, no significant relationship is observed between the $I_{\mathrm{W\text{-}UTA}}/n_\mathrm{e}$ and the presence or absence of the ITB. The tungsten density in the ITB phase exhibits a threshold limit of $I_{\mathrm{W\text{-}UTA}}/n_\mathrm{e} < 24$ (phs·m·s^{-1}·Sr^{-1}), at which the V_{t0} remains below 150 km·s^{-1}. In addition, the $I_{\mathrm{W\text{-}UTA}}/n_\mathrm{e}$ during the ITB phase is clearly lower than that during discharge phase without ITB. This suggests that impurity screening may be driven by the ion temperature gradient.

To assess the effect of ion temperature screening on the tungsten density, the statistical analysis is attempted using the same shots as figure 12(*a*). In EAST discharges, the T_i-ITB typically is formed at radial range of $\rho < 0.2$. For the purpose of evaluating the normalized characteristic length of the ion temperature gradient ($R/L_{T\mathrm{i}}$), two radial points in the plasma core are selected, i.e. $R_0 = 1.869$ m near the shoulder of the T_i-ITB (ρ_{shoulder}) and $R_1 = 2.038$ m near the foot of the T_i-ITB (ρ_{foot}). In the present statistical analysis three distinct conditions are considered; (1) discharges without T_i-ITB (with tungsten accumulation), (2) discharges without T_i-ITB (without tungsten accumulation) and (3) discharges with T_i-ITB. Multiple time points are recorded during a single discharge based on the discharge variation. As shown in figure 12(*a*), when $R/L_{T\mathrm{i}} < 2.5$, the tungsten ion density remains relatively high, i.e. $18 < I_{\mathrm{W\text{-}UTA}}/n_\mathrm{e}$ (phs·m·s^{-1}·Sr^{-1}) < 50, in discharges without ITB with tungsten accumulation. As $R/L_{T\mathrm{i}}$ increases, the tungsten accumulation can be effectively mitigated and leads to a significant decrease in the tungsten ion density of $I_{\mathrm{W\text{-}UTA}}/n_\mathrm{e} < 18$

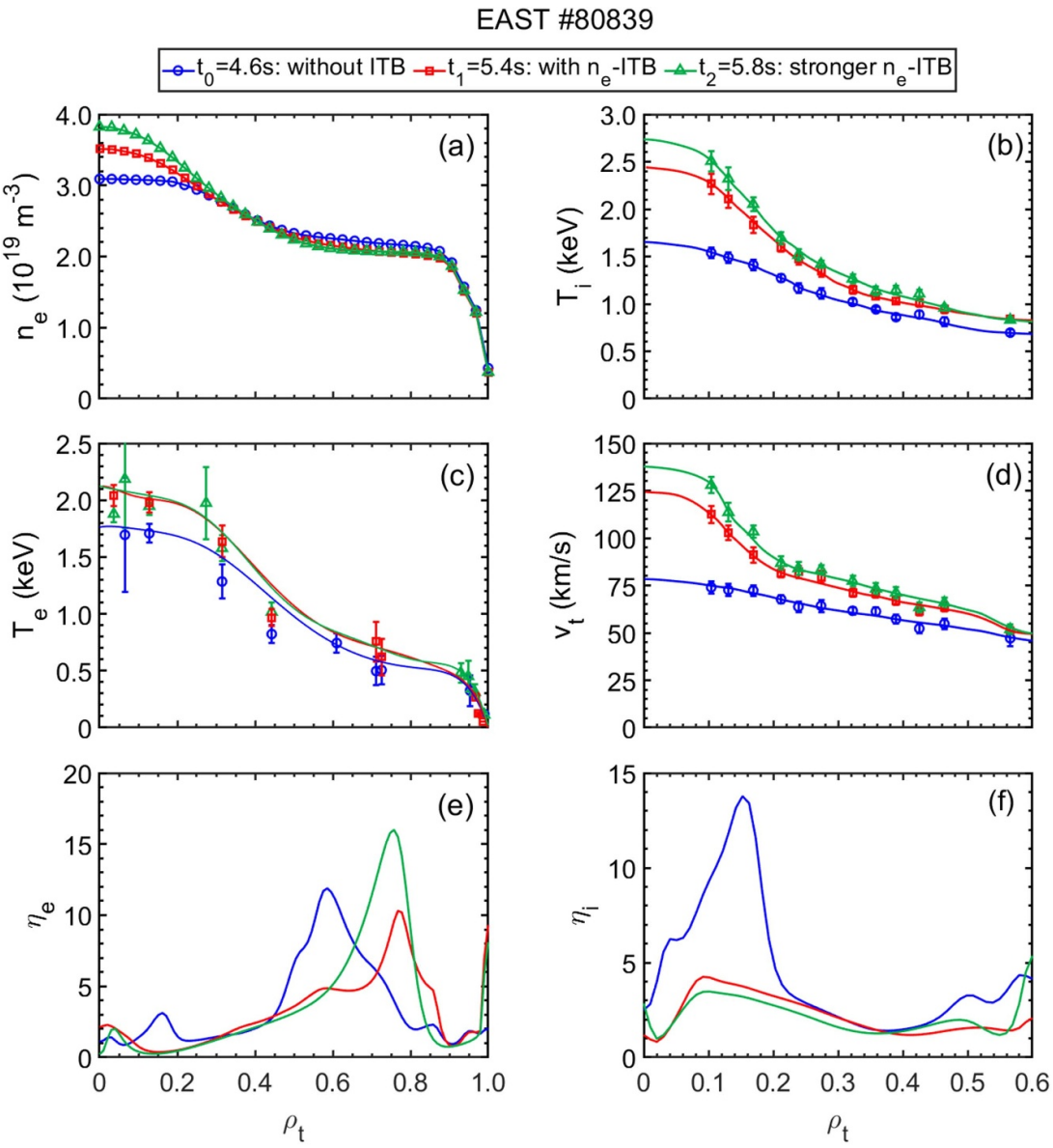

Figure 8. Radial profiles of (*a*) electron density, n_e, (*b*) ion temperature, T_i, (*c*) electron temperature, T_e, (*d*) toroidal rotation velocity, V_t, (*e*) ratio of logarithmic gradient of electron temperature to logarithmic gradient of density, η_e, and (*f*) ratio of logarithmic gradient of ion temperature to logarithmic gradient of density, η_i, at three timings in EAST #80839 discharge. Three discharge timings are indicated in figure 7 with vertical dash-dotted lines.

(phs·m·s^{-1}·Sr^{-1}). With the T_i-ITB formation (solid circles and diamonds in figure 12(*a*)), the tungsten ion density gradually increases as the value of R/L_{Ti} increases. This is because the T_i-ITB formation is generally accompanied by an increase in the electron density, leading to a slight tungsten accumulation through the density gradient effect. The present results indicate that the large R/L_{Ti} is one of the key factors in suppressing the accumulation of high-Z impurity ions, and effectively controlling the concentration in the plasma core.

It is noteworthy that during the T_i-ITB phase of discharge #71326, low-Z impurity ions exhibit a different transport from the high-Z impurity ions locating inside the ITB, as evidenced by the enhanced line emissions from low-Z impurity ions such as O^{7+} (see figure 4). This suggests that the origin dominating the transport of low-Z and high-Z impurity ions may differ. The relationship between $I_{O\,VIII}/n_e$ (O VIII at 18.970 Å) and both V_{t0} and R/L_{Ti} is illustrated in figures 11(*b*) and 12(*b*). The r and p presented in table 2 indicate no correlation between $I_{O\,VIII}/n_e$ and V_{t0} or R/L_{Ti}. To our knowledge, the centrifugal effect for low-Z impurity ions caused by the toroidal rotation velocity is weaker compared to that for high-Z impurity ions. Then, the dependence of the low-Z impurity accumulation on the toroidal rotation velocity is less pronounced than that of high-Z impurity accumulation. As for the temperature screening effect, its weak manifestation in low-Z impurities may be the result of a balance between two factors. First, as the T_i-ITB forms, the temperature screening effect reduces the inward convection of impurity particles. However, the formation of the T_i-ITB typically results from a reduction

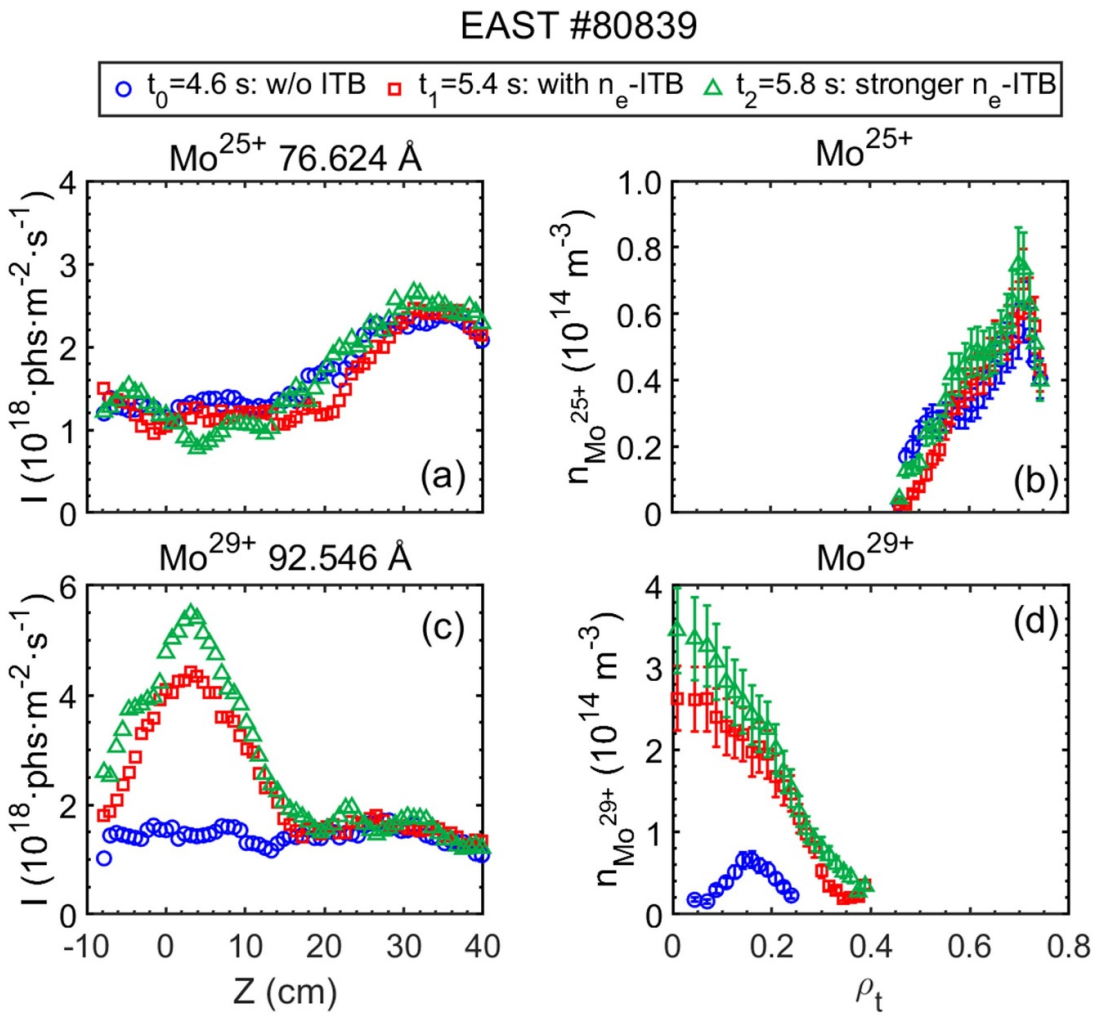

Figure 9. Radial profiles at three timings shown in figure 8, (*a*) vertical profile of line intensity of Mo^{25+} (1263–1320 eV) at 76.624 Å and (*b*) density profile of Mo^{25+} ion, and (*c*) vertical profile of line intensity of Mo^{29+} (1537–1587 eV) at 92.546 Å and (*d*) density profile of Mo^{29+} ion.

in low/middle-k turbulence, which, to some extent, decreases anomalous particle diffusion. Consequently, this leads to the statistical observation that the intensity of low-Z impurities shows no significant correlation with R/L_{Ti}. The differing behaviors of high-Z and low-Z impurities also suggest that, for high-Z impurities, the effect of turbulent transport is weaker than that of neoclassical transport.

4.2. Effect of electron density peaking

In the n_e-ITB phases, a significant increase in line emissions of high-Z impurity ions is observed inside the ITB (see figures 4, 5 and 9). Throughout this phase, the value of R/L_{Ti} is unchanged and V_{t0} decreases to 43 km·s^{-1} at $t = 4.45$ s. Then, it increases slightly to 57 km·s^{-1}, while R/L_{ne} rapidly increases from 3.4 to 4.9. The line intensity growth rate of the O^{7+} ion increases significantly compared to the previous phase, further indicating that strong electron density peaking effect substantially enhances the radiation of low-Z impurities which are inside the n_e-ITB. For high-Z impurities, according to the analysis in section 4.1, the transport of high-Z impurities inside the ITB is primary governed by neoclassical transport, where the competition between the effects of ion temperature screening and electron density peaking resulted in a reversal of impurity ion convection direction. After the formation of n_e-ITB, the strong electron density peaking effect surpasses the ion temperature screening effect, causing inward convection and promoting the accumulation of high-Z impurities. In addition, simulations by Shi *et al* [37] using the neoclassical transport code NEO and the turbulent transport code TGLF indicate that, inside the ITB region, turbulent transport was effectively suppressed, with neoclassical transport dominating. Consequently, the peaking of the electron density induced inward neoclassical convection, resulting in tungsten impurity accumulation on EAST [37]. Shi *et al* also simulated the accumulation of tungsten impurities by modifying the electron density profile, and their simulation results are consistent with the findings of this work, further confirming that the magnitude of η_i is a critical factor driving impurity accumulation.

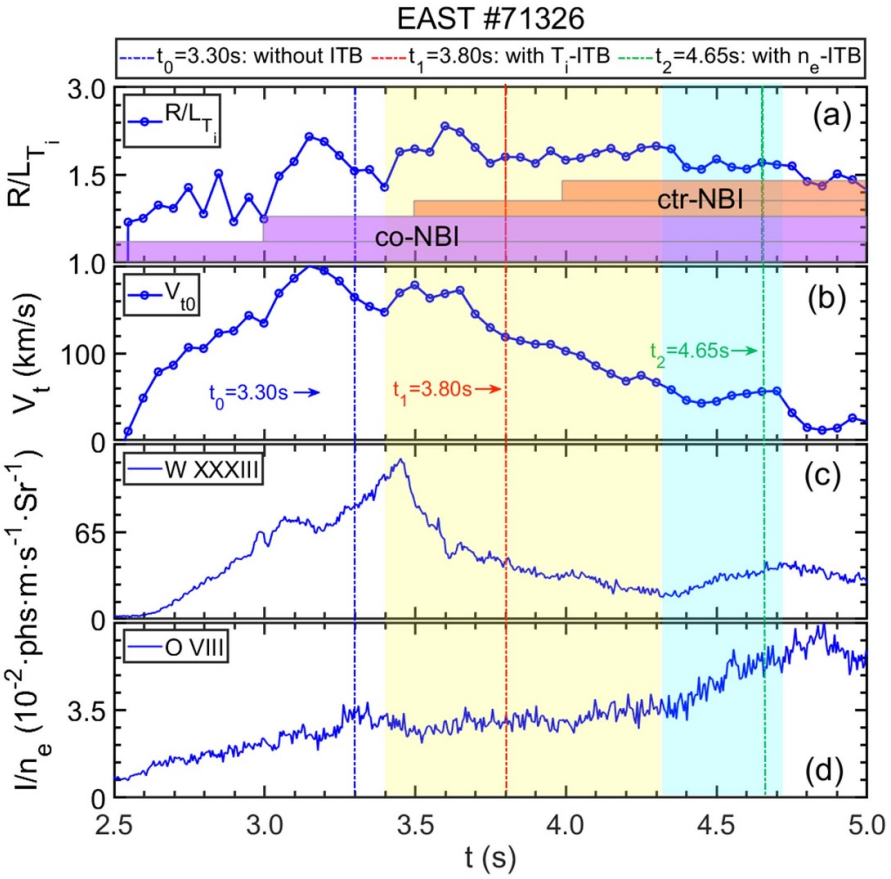

Figure 10. Time evolution of EAST discharge #71326, (*a*) normalized gradient of ion temperature, R/L_{Ti}, (*b*) core toroidal rotation velocity, V_{t0}, and impurity ion densities evaluated from a ratio of impurity line intensity to line-averaged electron density, I_{imp}/n_e, (*c*) $I_{W\ XXXIII}/n_e$ and (*d*) $I_{O\ VIII}/n_e$. Square frames represent duration of each NBI. Three discharge timings are indicated in figure 2 with vertical dash-dotted lines.

4.3. Impurity control strategy for fusion devices

The transport of high-Z and low-Z impurities in high β_N plasma with ITB offer critical insights for impurity control in fusion devices. The findings of this work indicate that electron density peaking effect promotes high-Z impurity accumulation, while ion temperature screening effect effectively mitigates it. Furthermore, the positive correlation between tungsten density and toroidal rotation velocity suggests that lower toroidal rotation velocity may contribute to a reduction in high-Z impurities accumulation in NBI-dominant discharges. However, the transport of low-Z impurities may be influenced by the combined effects of neoclassical and turbulent transport. For fusion devices, tungsten impurities, widely used as plasma-facing components, tend to accumulate in the plasma core, increasing radiation losses. Therefore, optimizing η_i and reducing the toroidal rotation velocity are crucial for controlling high-Z impurities accumulation. Considering that the density in future fusion devices will inevitably peak [38], regulating the ion temperature profile plays an essential role. In future fusion devices, controlling the current profile to achieve a reversed *q*-profile will facilitate the formation of ITBs. In such a scenario, the formation of ITBs does not rely on strong toroidal rotation, thereby effectively avoiding impurity accumulation caused by rotational effects. By broadening the current profile to form a wider ITB, the temperature screening effect can be fully utilized while flattening the core density profile. This state may represent an ideal scenario for future fusion devices to mitigate impurity accumulation.

5. Summary

The transport of intrinsic high-Z (Fe, Cu, Mo and W) and low-Z (C and O) impurity ions in high β_N discharges with ITB is investigated in detail, utilizing the fast-time-response and space-resolved EUV spectrometer systems developed on the EAST. The analysis mainly focuses on impurity behavior during the T_i-ITB and n_e-ITB phases. Experimental results show that the line radiation of low-Z impurity ions like O^{6+} and high-Z impurity ions like Fe^{17+} and Mo^{25+} locating between ITB foot and pedestal top remains unchanged during the ITB phase. However, transport of the high-Z impurity ions locating inside the ITB is predominantly governed by neoclassical transport mechanism, i.e. determined by balance between

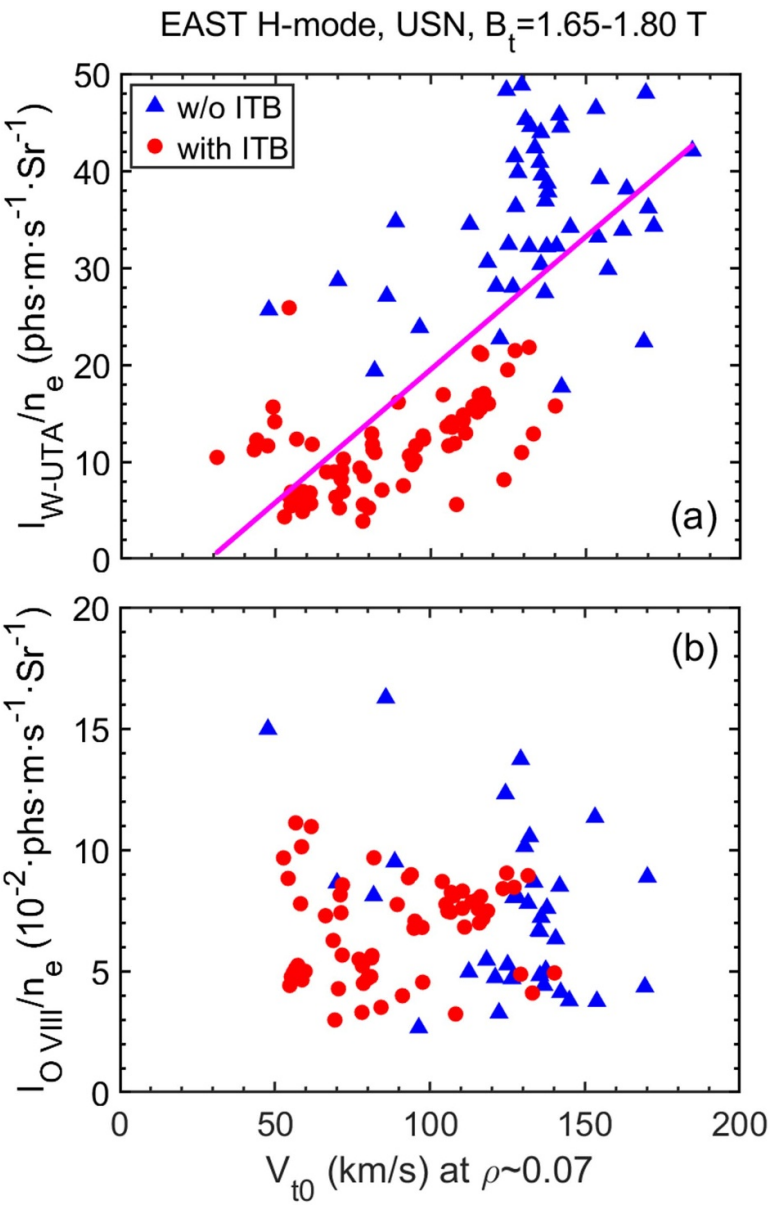

Figure 11. Low- and high-Z impurity ion densities evaluated from a ratio of impurity line intensity to line-averaged electron density, I_{imp}/n_e, against central toroidal rotation velocity, V_{t0} at $\rho \sim 0.07$; (*a*) tungsten density, $I_{W\text{-}UTA}/n_e$, and (*b*) oxygen density, $I_{O\ VIII}/n_e$. Solid blue triangles and red circles indicate data from discharges without ITB and with T_i-ITB, respectively. Magenta line is the linear fitting result.

Table 2. Correlation analysis of low- and high-Z impurities with toroidal rotation velocity and ion temperature gradients.

Comparison of analyzed variables	Pearson Correlation Coefficient (r)	Significance Level (p)	Correlation
V_{t0} vs $I_{W\text{-}UTA}/n_e$	0.743	1.23×10^{-16}	positive correlation
V_{t0} vs $I_{O\ VIII}/n_e$	−0.045	0.89	no correlation
R/L_{Ti} vs $I_{W\text{-}UTA}/n_e$	−0.611	1.34×10^{-8}	negative correlation
R/L_{Ti} vs $I_{O\ VIII}/n_e$	−0.116	0.72	no correlation

Notes: $r \in [-1,1]$. $r = 0$ implies no correlation; values of r closer to 1 or −1 indicate stronger positive or negative correlations, respectively.
$p \in [0,1]$. Typically, $p < 0.05$ indicates a statistically significant correlation.

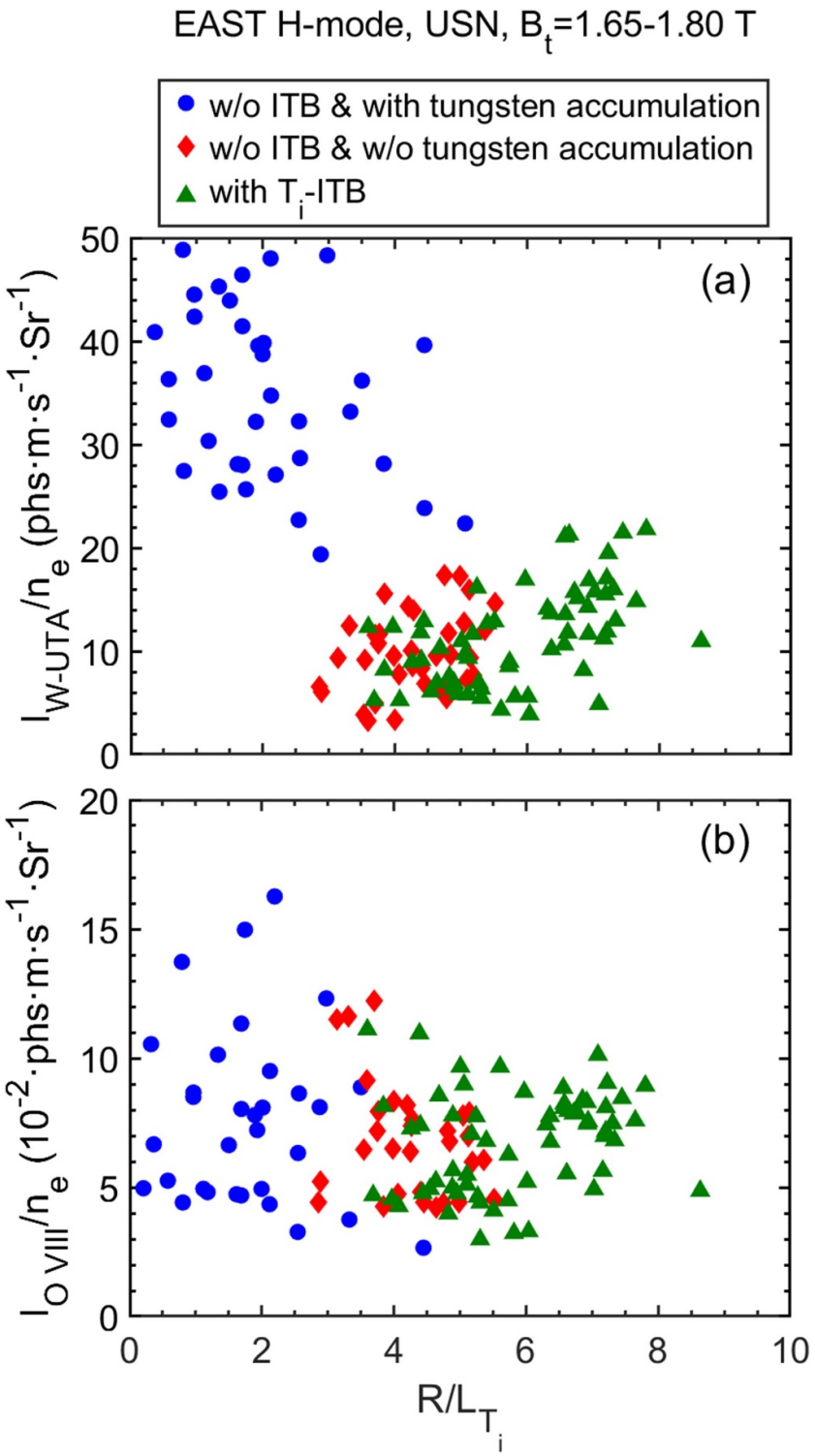

Figure 12. Impurity ion density of (*a*) tungsten, $I_{\text{W-UTA}}/n_e$, and (b) oxygen, $I_{\text{O VIII}}/n_e$, as a function of normalized gradient of ion temperature, $R/L_{T\text{i}}$. Calculation for the plot is done using T_i at $R_0 = 1.869$ m and $R_1 = 2.038$ m, normalized to the major radius, $R = 1.9$ m; blue solid circles: without T_i-ITB (with tungsten accumulation), red solid diamonds: without T_i-ITB (without tungsten accumulation) and green solid triangles: with T_i-ITB.

electron density and ion temperature gradients. During the T_i-ITB phase, the dominance of the ion temperature gradient drove the impurity convection outward, resulting in a significant screening of the high-Z impurity ions. The present observation demonstrated reduction of the line radiation of Fe^{22+}, Cu^{21+}, Cu^{25+}, Mo^{30+}, W^{27+} and W^{32+} ions and notably flattened radial density profiles of W^{27+}, W^{29+} and W^{37+}. We also observed that the electron density gradient increased

from $R/L_{ne} = 3.4$ to 4.9 and η_i decreased during n_e-ITB phase drove the impurity ions inward, leading to the impurity accumulation, in particular, for tungsten ions.

In contrast to this, low-Z impurity ions like O^{7+} exhibit different transport during the T_i-ITB phase. Based on these observations, statistical analysis on the impurity density is conducted against the toroidal rotation velocity and ion temperature gradient to investigate the correlation among V_{t0}, R/L_{Ti}, $I_{W\text{-}UTA}/n_e$ and $I_{O\ VIII}/n_e$. The result indicated that a positive correlation exists between toroidal rotation velocity and tungsten density regardless of whether an ITB forms or not. The $I_{W\text{-}UTA}/n_e$ was low during ITB phase, e.g. $I_{W\text{-}UTA}/n_e \leqslant 24$ (phs·m·s^{-1}·Sr^{-1}) at $V_{t0} \leqslant 150$ km·s^{-1}. The tungsten accumulation frequently occurred when R/L_{Ti} was below 2.5, where $I_{W\text{-}UTA}/n_e$ ranged between 18 and 50 (phs·m·s^{-1}·Sr^{-1}). Unlike high-Z impurity ions, low-Z impurity ions like O^{7+} show no significant correlation with toroidal rotation velocity and ion temperature gradient in the statistical analysis.

The present experimental study in high β_N discharges highlighted that tungsten impurity accumulation and concentration can be effectively suppressed by optimizing the plasma parameters (V_t and η_i) and controlling the current profile, which are essential for realizing a wide variety of plasma operations and maintaining high pressure discharges with ITB in fusion devices with tungsten material as the plasma-facing component. In addition, these findings are applicable to future experiments on EAST. With the EAST being planned for further exploration of high-confinement long-pulse steady-state operation, the results of this study can provide guidance for impurity control in the high-confinement scenarios during such exploration on EAST.

Acknowledgment

This work was supported by the National Magnetic Confinement Fusion Energy R&D Program of China (Grant Nos. 2022YFE03020004, 2022YFE03180400 and 2024YFE03000200), National Natural Science Foundation of China (Grant Nos. 12322512 and 12275315), Chinese Academy of Sciences President's International Fellowship Initiative (PIFI) (Grant Nos. 2025PVA0060 and 2024PVA0074), and the Science Foundation of Institute of Plasma Physics, Chinese Academy of Sciences (Grant No. DSJJ-2024-08). We thank the staff members at EAST (https://cstr.cn/31130.02.EAST), for providing technical support and assistance in data collection and analysis.

ORCID iDs

Wenmin Zhang https://orcid.org/0009-0000-9980-6765
Ling Zhang https://orcid.org/0000-0001-7880-9588
Yuqi Chu https://orcid.org/0000-0002-7379-0117
Shigeru Morita https://orcid.org/0000-0003-4139-7721
Xiang Gao https://orcid.org/0000-0003-1885-2538
Gongshun Li https://orcid.org/0000-0002-5542-1238
Shouxin Wang https://orcid.org/0000-0001-9600-4038
Yunxin Cheng https://orcid.org/0000-0002-9195-2757
Yingying Li https://orcid.org/0000-0002-2978-908X
Chengxi Zhou https://orcid.org/0000-0001-9200-1665
Darío Mitnik https://orcid.org/0000-0003-0193-0958
Zhen Zhou https://orcid.org/0009-0000-8261-7837
Ning Yan https://orcid.org/0000-0002-2536-5853
Haiqing Liu https://orcid.org/0000-0001-6892-358X
Guosheng Xu https://orcid.org/0000-0001-8495-8678

References

[1] Rodriguez-Fernandez P. *et al* 2022 *Nucl. Fusion* **62** 042003
[2] Bigot B. *et al* 2019 *Nucl. Fusion* **59** 112001
[3] Shimada M. *et al* 2007 *Nucl. Fusion* **47** S1–S7
[4] Sips A.C.C. *et al* 1998 *Plasma Phys. Control. Fusion* **40** 647
[5] Fiore C.L. *et al* 2001 *Phys. Plasmas* **8** 2023–8
[6] Rice J.E. *et al* 2002 *Nucl. Fusion* **42** 510
[7] Sakamoto Y. *et al* 2001 *Nucl. Fusion* **41** 865
[8] Ding S. *et al* 2017 *Phys. Plasmas* **24** 056114
[9] Conway G.D. *et al* 2001 *Plasma Phys. Control. Fusion* **43** 1239
[10] Chung J. *et al* 2018 *Nucl. Fusion* **58** 016019
[11] Deng W. *et al* 2002 *Phys. Plasmas* **29** 102106
[12] Gao X. *et al* 2020 *Nucl. Fusion* **60** 102001
[13] Chu Y.Q. *et al* 2021 *Plasma Phys. Control. Fusion* **63** 105003
[14] Ge W.L., Wang Z.X., Wang F., Liu Z. and Xu L. 2022 Nucl. *Fusion* **63** 016007
[15] Yu L. *et al* 2024 *Plasma Phys. Control. Fusion* **66** 115006
[16] Loarte A. *et al* 2007 *Nucl. Fusion* **47** S203–63
[17] Dux R. *et al* 2003 *J. Nucl. Mater.* **313–316** 1150
[18] Dux R., Giroud C. and Zastrow K.-D. and (JET EFDA contributors) 2004 *Nucl. Fusion* **44** 260–4
[19] Takenaga H. *et al* 2003 *Nucl. Fusion* **43** 1235
[20] Ida K. *et al* 2009 *Phys. Plasmas* **16** 056111
[21] Ida K. and Fujita T. 2018 *Plasma Phys. Control. Fusion* **60** 03300
[22] Zhang W.M. *et al* 2022 *Phys. Scr.* **97** 045604
[23] Zhang W.M. *et al* 2024 *Phys. Scr.* **99** 105609
[24] Li L. *et al* 2021 *Plasma Sci. Technol.* **23** 075102
[25] Gao X. *et al* 2017 *Nucl. Fusion* **57** 056021
[26] Li Y.Y. *et al* 2014 *Rev. Sci. Instrum.* **85** 11E428
[27] Qing Z., Junyu Z., Li Y., Qingsheng H., Yanqing J., Tao Z., Xiaoqi X., Bhatti S.H. and Xiang G. 2010 *Plasma Sci. Technol.* **12** 144
[28] Han X., Liu X., Liu Y., Domier C.W., Luhmann N.C., Li E.Z., Hu L.Q. and Gao X. 2014 *Rev. Sci. Instrum.* **85** 073506
[29] Liu H.Q. *et al* 2016 *Rev. Sci. Instrum.* **87** 11D903
[30] Zhang L. *et al* 2015 *Rev. Sci. Instrum.* **86** 123509
[31] Xu Z. *et al* 2021 *Nucl. Instrum. Methods Phys. Res.* A **1010** 165545
[32] Zhang L. *et al* 2019 *Nucl. Instrum. Methods Phys. Res.* A **916** 169–78
[33] Wu M.F. *et al* 2020 *Plasma Sci. Technol.* **22** 025102
[34] Gu M.F. *et al* 2008 *Can. J. Phys.* **86** 675
[35] Cheng Y.X. *et al* 2022 *IEEE Trans. Plasma Sci.* **50** 691–9
[36] Fajardo D., Angioni C., Kim S.H., Koechl F., Fable E., Loarte A., Polevoi A. and Tardini G. 2025 *Plasma Phys. Control. Fusion* **67** 015020
[37] Shi S.Y. *et al* 2022 *Nucl. Fusion* **62** 066032
[38] Angioni C., Peeters A.G., Pereverzev G.V., Ryter F. and Tardini G. 2003 *Phys. Rev. Lett.* **90** 205003